Alternative discretization in the numerical renormalization-group method

Vivaldo L. Campo, Jr. and Luiz N. Oliveira
Departamento de Física e Informática, Instituto de Física de São Carlos, Universidade de São Paulo, Caixa Postal 369, 13560-970 São Carlos, São Paulo, Brazil
(Received 17 May 2005; published 23 September 2005)

A logarithmic discretization procedure, alternative to the one traditionally employed in the Numerical renormalization-group computations of physical properties for impurity models, is introduced. While the traditional method neglects the coupling of the conduction states most localized around the impurity site to all other conduction states, this one constructs a nonorthogonal basis that diagonalizes the conduction-band Hamiltonian and neglects the overlap between basis states. Unlike the traditional procedure, which underestimates the spectral density of the coupling between the conduction band and the impurity, this one requires no *ad hoc* renormalization of coupling constants. Numerical examples covering the specific heat for the Kondo model and the impurity spectral densities for the uncorrelated Anderson model show that, for the same discretization parameters, this procedure is substantially more accurate than the traditional one.

DOI: 10.1103/PhysRevB.72.104432 PACS number(s): 75.20.Hr, 75.30.Hx

I. INTRODUCTION

The numerical renormalization group (NRG) computation of the magnetic susceptibility for the Kondo model, a breakthrough combining analytical arguments with an unconventional numerical approach involving strictly controllable approximations, finds few parallels in condensed-matter theory.[1] In the three decades that have followed this development, one counts numerous calculations of thermodynamical, dynamical or transport properties for different impurity models, based on the NRG procedure.[2–12] The original work was concerned with universal properties and paid little attention to irrelevant operators, which in the single-impurity Kondo Hamiltonian affect the low-temperature properties only to the extent that they change the Kondo temperature T_K.[1] Later interest in nonuniversal curves led to generalizations, which nonetheless preserved an essential feature of the method: the logarithmic discretization of the conduction band. Even those that modified the logarithmic sequence[6] left untouched the association of a discrete basis with the logarithmic mesh, and to justify the discretization, all NRG calculations have relied on rapid convergence of the calculated physical properties to the continuum.

Many of the above-mentioned generalizations have succeded in accelerating that convergence, so that calculations with relatively coarse meshes have yielded physical properties within a few percent of the continuum limit. An early landmark was established in Ref. 3, which showed that, to ensure fast convergence of nonuniversal properties, one must renormalize all impurity-band couplings by mesh-dependent factors. That empirical finding received support from the analytical diagonalization of simple Hamiltonians and the numerical diagonalization of a number of more complex ones, including the two-impurity Kondo Hamiltonian, with its energy-dependent couplings.[10]

While attempting to compute the specific heat for the two-impurity Kondo model,[13] we were surprised by unusually slow convergence to the continuum limit. As the data in Sec. VII will show, in marked contrast with computations for the single-impurity Kondo model, numerical results for the impurity-added contribution to the specific heat computed with coarse logarithmic meshes are in only qualitative agreement with the continuum curves.

A milder version of the same difficulty appears when the impurity spectral density for the two-impurity Anderson model is computed with coarse meshes. As the results in Sec. VIII will show, even for the uncorrelated model, in which case the two-impurity Hamiltonian decouples into two single-impurity Anderson Hamiltonians with energy-dependent impurity-band couplings, the discrepancy between the coarse-mesh and the continuum spectral densities is significant.

These findings prompted us to seek an alternative definition of the discrete basis, the result of which is the subject of this paper. Our construction eliminates the *ad hoc* renormalization of coupling constants and accelerates the convergence to the continuum of physical properties for the two-impurity model. As an illustration, we show that our method yields temperature-dependent specific heat curves free from the artificial oscillations found in those calculated by the traditional method.[13,17]

The paper is organized as follows. Section II defines the model Hamiltonian that will illustrate our presentation. Sections III and IV compare the construction of the discretized basis for a linear mesh with that for a nonlinear mesh and identify the origin of deviations. Section V then shows that an alternative definition of that basis eliminates such deviations. The two-impurity model is described in Sec. VI, and numerical results for its specific heat and spectral densities are presented in Secs. VII and VIII, respectively. Finally, Sec. IX summarizes our conclusions.

II. MODEL HAMILTONIAN

For definiteness, our discussion of the conduction-band discretization will make reference to an Anderson model with energy-dependent coupling, comprising a localized spin-degenerate orbital c_{imp} and a structureless, half-filled, noninteracting conduction band with energies ϵ, measured

from the Fermi level, ranging from $-D$ to D. In standard notation, the Hamiltonian is

$$H_A = \int \epsilon c_\epsilon^\dagger c_\epsilon \, d\epsilon + A(f_0^\dagger c_{\rm imp} + {\rm H.c.}) + \epsilon_{\rm imp} n^{\rm imp} + U n_\uparrow^{\rm imp} n_\downarrow^{\rm imp}, \tag{1}$$

where $n^{\rm imp} \equiv c_{\rm imp}^\dagger c_{\rm imp}$ denotes the occupation of the localized level, $\epsilon_{\rm imp}$ is the impurity-orbital energy, U is the Coulomb repulsion between electrons occupying the impurity orbital, the operator f_0 is defined by

$$A f_0 \equiv \int_{-D}^{D} \sqrt{\frac{\Gamma(\epsilon)}{\pi}} c_\epsilon \, d\epsilon, \tag{2}$$

and the constant A ensures that $\{f_0, f_0^\dagger\} = 1$:

$$A = \sqrt{\int_{-D}^{D} \frac{\Gamma(\epsilon)}{\pi} d\epsilon}. \tag{3}$$

III. LINEAR DISCRETIZATION

In order to identify the source of the deviations introduced by the logarithmic discretization of the conduction band, this section discusses a more conventional numerical approach to the computation of the physical properties for the Hamiltonian (1), one in which the conduction band is linearly discretized. Mathematically, the first term on the right-hand side of Eq. (1) is equivalent to the Hamiltonian for a lattice with an arbitrarily large number, $2N$, of sites, extending from $x = 0$ to $x = (2N-1)a$, with appropriate couplings between the sites. Upon this lattice, we impose twisted boundary conditions, i.e., require the wave function $\psi(x)$ to satisfy

$$\psi(x = 0) = \psi(2Na) \exp(i 2\pi z), \tag{4}$$

with an arbitrary twist parameter z in the interval $0 < z \leq 1$.

We will be interested in momenta in the positive half of the Brillouin zone, i.e., $0 < k \leq \pi/a$, in which N finely spaced discrete states are allowed:

$$k = \frac{\pi}{a}\left(1 - \frac{n + z - 1}{N}\right) \quad (n = 1, 2, \ldots, N). \tag{5}$$

With $N \to \infty$, momentum sums become energy integrals, $(1/2N)\Sigma_{k,\sigma} \to \int \rho(\epsilon) d\epsilon$. To mimic the model in Sec. II, we will consider a band extending from $\epsilon_{k=0} \equiv -D$ to $\epsilon_{k=\pi/a} \equiv D$, with a linear dispersion relation, $\epsilon_k = (2Da/\pi)(k - \pi/2a)$. Two spin components accounted for, the per-allowed-momentum density of states is then constant, $\rho(\epsilon) = 1/2D$.

A coarser discretization requires a mesh analogous to Eq. (5):

$$k_1 = \frac{\pi}{a}, \tag{6}$$

$$k_j = \frac{\pi}{a}\left(1 - \frac{j + z - 2}{2\mathcal{J}}\right) \quad (j = 2, 3, \ldots, 2\mathcal{J} + 1), \tag{7}$$

where M is a large integer such that $\mathcal{J} \equiv N/2M$ is also integer and remains constant as $N \to \infty$. By letting z run from zero to unity, we cover all momenta in Eq. (5). The corresponding points in energy space are

$$\epsilon_1^z = D \tag{8}$$

and

$$\epsilon_j^z = D\left(1 - \frac{j + z - 2}{\mathcal{J}}\right) \quad (j = 2, 3, \ldots, 2\mathcal{J} + 1) \tag{9}$$

or

$$\epsilon_j^z = D - (j + z - 2)\Delta \quad (j = 2, 3, \ldots, 2\mathcal{J} + 1), \tag{10}$$

where $\Delta = D/\mathcal{J}$ is the energy separation defining the mesh.

For each of the mesh intervals $I_j = [\epsilon_{j+1}^z, \epsilon_j^z]$ $(j = 1, 2, \ldots, \mathcal{J})$, we now consider an orthonormal set of functions:

$$\phi_{jm}(\epsilon) = \frac{\exp[2\pi i m \epsilon/(\epsilon_j^z - \epsilon_{j+1}^z)]}{(\epsilon_j^z - \epsilon_{j+1}^z)^{1/2}} \quad (m \text{ integer}), \tag{11}$$

so that

$$\int_{I_j} \phi_{jm}^*(\epsilon) \phi_{jm'}(\epsilon) d\epsilon = \delta_{m,m'}. \tag{12}$$

This leads naturally to an orthonormal basis of Fermi operators:

$$b_{jm} = \int_{I_j} \phi_{jm}(\epsilon) c_\epsilon \, d\epsilon. \tag{13}$$

Inverted, Eq. (13) yields the exact relation

$$c_\epsilon = \sum_{m=-\infty}^{\infty} \phi_{jm}(\epsilon) b_{jm} \quad (\epsilon \in I_j). \tag{14}$$

For practical applications, the infinite number of operators makes the basis of the b_{jm} unwieldy. A more convenient, albeit incomplete basis results from disregarding all but the leading operator, b_{j0}, in each interval I_j.

In the negative half of the conduction band, instead of relying on the twisted condition (4), we find it more convenient to choose a mesh comprising energies symmetric to the sequence in Eq. (10) and more practical to denote those energies by negative indices:

$$\epsilon_{-j}^z \equiv -D + (j + z - 2)\Delta \quad (j = 2, 3, \ldots, \mathcal{J} + 1). \tag{15}$$

We can now project the model Hamiltonian H_A on the basis of the operators b_{j0}. We postpone the case of energy-dependent coupling to Sec. VI and will consider, for simplicity, an energy-independent coupling $\Gamma(\epsilon) \equiv \Gamma$, so that the normalization constant $A = \sqrt{2D\Gamma/\pi}$.

Substitution of Eq. (14) on the right-hand side of Eq. (1) yields

$$H_A = \sum_{j=1}^{\mathcal{J}} E_j^z (b_{j0}^\dagger b_{j0} - b_{-j0}^\dagger b_{-j0}) + \sqrt{2D\Gamma/\pi}(f_0^\dagger c_{\mathrm{imp}} + \mathrm{H.c.}) + \epsilon_{\mathrm{imp}} n^{\mathrm{imp}} + U n_\uparrow^{\mathrm{imp}} n_\downarrow^{\mathrm{imp}}, \tag{16}$$

where

$$E_j^z = \int_{I_j} \epsilon\, d\epsilon \Big/ \int_{I_j} d\epsilon, \tag{17}$$

i.e.,

$$E_j^z = (\epsilon_j^z + \epsilon_{j+1}^z)/2 \quad (j = 1, \ldots, \mathcal{J}), \tag{18}$$

or according to Eqs. (10) and (15),

$$E_1^z = D - z\Delta/2, \tag{19}$$

$$E_j^z = D - (j + z - 3/2)\Delta \quad (j = 2, \ldots, \mathcal{J}). \tag{20}$$

Although Eq. (20) would have followed directly from imposing the twisted periodic condition (4), with a twist $z + 1/2$ instead of z, on a sample with $\mathcal{J}$ sites [cf. Eq. (10)], the sequence of Eqs. (9)–(20) will prove important, for unlike the twisted boundary condition, it can generate nonlinear discretizations.

Before turning to other meshes, we note that the discrete basis $\{b_{j0}\}$ satisfies one of the requirements of the NRG approach,[1,2] namely, it is possible to write, exactly, the operator f_0, defined by Eq. (2), as a linear combination of the basis operators:

$$f_0 = \sum_{j=1}^{\mathcal{J}} \sqrt{\frac{|\epsilon_j^z - \epsilon_{j+1}^z|}{2D}}(b_{j0} + b_{-j0}), \tag{21}$$

so that, while the discretization affects the conduction-band Hamiltonian, it does not affect its coupling to the impurity. Moreover, as we shall now show, in the decoupled conduction-band limit, i.e., for $\Gamma \to 0$, it does not affect the spectral density of the operator f_0,

$$\rho_0(\epsilon, z) = \sum_\alpha |\langle \alpha | f_0^\dagger | \Omega \rangle|^2 \delta(E_\alpha - E_\Omega - \epsilon), \tag{22}$$

where $|\Omega\rangle$ and $|\alpha\rangle$ are the ground state and an eigenstate of the conduction-band Hamiltonian, with eigenvalues E_Ω and E_α, respectively, calculated for a given twist z.

The matrix element on the right-hand side of Eq. (22) will vanish unless $|\alpha\rangle = b_{j0}^\dagger |\Omega\rangle$ for some j $(j = 1, \ldots, \mathcal{J})$. It follows that $E_\alpha = E_\Omega + E_j^z$ and $\langle \alpha | f_0^\dagger | \Omega \rangle = \{b_{j0}, f_0^\dagger\}$. Equation (21) yields the anticommutator, and we find that

$$\rho_0(\epsilon, z) = \sum_j \frac{\epsilon_j^z - \epsilon_{j+1}^z}{2D} \delta(E_j^z - \epsilon). \tag{23}$$

The δ functions on the right-hand side result in a spiked spectral density, which reflects the discretization of the conduction states. In order to recover the continuum, that is, to cover all momenta in the conduction band, we must integrate both sides of Eq. (23) over the twist z. We therefore compute

$$\rho_0(\epsilon) = \int_0^1 \rho_0(\epsilon, z) dz, \tag{24}$$

which yields

$$\rho_0(\epsilon) = \frac{\epsilon_j^z - \epsilon_{j+1}^z}{2D |dE_j^z/dz|_{E_j^z = \epsilon}}. \tag{25}$$

Equations (19) and (20) show that, for $-D < \epsilon < D$, one can always find $j (j = 1, 2, \ldots, \mathcal{J})$ and $z (0 < z \leqslant 1)$ such that $E_j^z = \epsilon$. The latter equality moreover yields

$$|dE_j^z/dz| = \Delta = \epsilon_j^z - \epsilon_{j+1}^z, \tag{26}$$

and hence

$$\rho_0(\epsilon) = 1/2D. \tag{27}$$

Trivially extended to the continuum, $\lim_{\Delta \to 0} \rho_0(\epsilon) = 1/2D$, Eq. (27) is exact for any discretization interval Δ. We see that Eqs. (9) and (15) preserve the spectral density of f_0, i.e., they preserve the coupling to the impurity. The linear discretization complies fully with one of the two requirements of the NRG approach.

Unfortunately, it fails to comply with the other requirement, since the discretization interval Δ is an artificial energy that breaks the scale invariance of the conduction band. This brings us to the logarithmic mesh.

IV. LOGARITHMIC DISCRETIZATION

The logarithmic mesh, designed to preserve the energy-scale invariance of the conduction band, comprises two sequences, of states above and below the Fermi level, respectively.[1,2,6] For our purposes, it will be sufficient to give attention to the positive energies, $0 < \epsilon \leqslant D$. We define the mesh as

$$\epsilon_1^z = D \tag{28}$$

and

$$\epsilon_j^z = D\Lambda^{2-j-z} \quad (j = 2, 3, \ldots). \tag{29}$$

The energy intervals $I_j^z \equiv [\epsilon_{j+1}^z, \epsilon_j^z]$ are then defined, and we can follow the steps leading from Eq. (11) to Eq. (18). For $j \geqslant 2$, for instance, the latter becomes

$$E_j^z = D\Lambda^{2-j-z}(1 + \Lambda^{-1})/2 \quad (j = 2, 3, \ldots). \tag{30}$$

Next, to calculate the spectral density ρ_0, we start at Eq. (21), which leads to Eq. (25). Now, however, the derivative on the right-hand is no longer equal to the discretization interval. For $j \geqslant 2$,

$$\left| \frac{dE_j^z}{dz} \right| = D \frac{1 + \Lambda^{-1}}{2} \Lambda^{2-j-z} \ln \Lambda, \tag{31}$$

and since

$$\epsilon_j^z - \epsilon_{j+1}^z = D(1 - \Lambda^{-1})\Lambda^{2-j-z}, \tag{32}$$

we find that

$$\rho_0(\epsilon) = \frac{1}{2DA_\Lambda}, \tag{33}$$

where

$$A_\Lambda = \frac{\ln \Lambda}{2} \frac{1+\Lambda^{-1}}{1-\Lambda^{-1}} \tag{34}$$

is the renormalization factor introduced in Ref. 3 to accelerate the convergence to the continuum limit of calculated thermodynamic properties.

Only in the continuum limit, $\Lambda \to 1$, does A_Λ equal unity, and only in that limit does Eq. (33) become exact. For $\Lambda > 1$, the deviation in the spectral density is equivalent to a renormalization of the constant multiplying f_0 in the Hamiltonian (1), i.e., a renormalization of the the level width Γ by A_Λ that affects the calculation of all impurity-added properties.[14]

Comparison with Sec. III shows that this renormalization is a consequence of the nonlinear relation between the interval limits ϵ_j^z and the twist parameter z. To see this, in the calculation of dE_j^z/dz, differentiate Eq. (17) . Since the lower and upper limits of the integrals on the right-hand side are ϵ_{j+1}^z and ϵ_j^z, respectively, the differentiation introduces energy-dependent factors $d\epsilon_{j+1}^z/dz = -\epsilon_{j+1}^z \ln \Lambda$ and $d\epsilon_j/dz = -\epsilon_j^z \ln \Lambda$, different from the constant $d\epsilon_{j+1}^z/dz = d\epsilon_j/dz = -\Delta$ in Sec. III [cf. Eq. (10)]. This considered, the renormalization of coupling constants by A_Λ may seem to be an inevitable undesirable consequence of the logarithmic mesh. Section V nonetheless shows that an alternative discretization avoids this problem.

V. ALTERNATIVE DEFINITION OF THE DISCRETE BASIS

Consider again the logarithmic mesh defined by Eqs. (28) and (29). For given j, we will now define a set of new basis functions φ_{jm} (m integer), all but one of which will differ from the ϕ_{jm} defined in Sec. III. The exception is the leading function φ_{j0}, identical to the one defined by Eq. (11):

$$\varphi_{j0}(\epsilon) \equiv \phi_{j0}(\epsilon) = (\epsilon_j^z - \epsilon_{j+1}^z)^{-1/2}. \tag{35}$$

To construct the remaining functions, we require that they obey the orthonormality condition with a modified scalar product:

$$\int_{I_j} \varphi_{jm}^*(\epsilon) g(\epsilon) \varphi_{jm'}(\epsilon) d\epsilon = \delta_{m,m'}. \tag{36}$$

For now, the weight function $g(\epsilon)$ is constrained only by the condition

$$\int_{I_j} g(\epsilon) d\epsilon = \epsilon_j^z - \epsilon_{j+1}^z, \tag{37}$$

which follows from Eq. (36) with $m' = m = 0$ and our definition of φ_{m0}, Eq. (35).

We next define a nonorthogonal basis comprising the operators

$$a_{jm} = \int_{I_m} \varphi_{jm}(\epsilon) c_\epsilon d\epsilon. \tag{38}$$

The a_{j0}, in particular, are identical to the b_{j0} defined in Eq. (13), and in analogy with Eq. (21), we have that

$$f_0 = \sum_{j=1}^{\infty} \sqrt{\frac{\epsilon_j^z - \epsilon_{j+1}^z}{2D}} (a_{j0} + a_{-j0}). \tag{39}$$

The inversion of Eq. (38) yields

$$c_\epsilon = \sum_{m=-\infty}^{\infty} g(\epsilon) \varphi_{jm}(\epsilon) a_{jm} \quad (\epsilon \in I_j), \tag{40}$$

It is then straightforward to project the model Hamiltonian on the new basis, and we find that

$$H_A = \sum_{jmm'} \mathcal{A}_{mm'}^j a_{jm}^\dagger a_{jm'} + \sqrt{2D\Gamma/\pi}(f_0^\dagger c_{\rm imp} + \text{H.c.}) + \epsilon_{\rm imp} n^{\rm imp} + U n_\uparrow^{\rm imp} n_\downarrow^{\rm imp}, \tag{41}$$

where the conduction-band matrix elements are

$$\mathcal{A}_{mm'}^j = \int \varphi_{jm}^*(\epsilon) \epsilon g^2(\epsilon) \varphi_{jm'}(\epsilon) d\epsilon, \tag{42}$$

for $j = \pm 1, \pm 2, \ldots$ and $m, m' = 0, 1, \ldots$. Comparison with Eq. (36) shows that the right-hand side will be diagonal if $\epsilon g^2(\epsilon) \propto g(\epsilon)$, i.e., if

$$g(\epsilon) = \mathcal{E}_j^z/\epsilon, \tag{43}$$

with a constant $\mathcal{E}_j^z$ determined by the constraint (37), which we can write

$$\mathcal{E}_j^z = \frac{\int_{I_j} d\epsilon}{\int_{I_j} d\epsilon/\epsilon}. \tag{44}$$

The integrals on the right-hand side are easily computed, and we find that

$$\mathcal{E}_{\pm 1}^z = \pm D \frac{1-\Lambda^{-z}}{z \ln \Lambda} \tag{45}$$

and

$$\mathcal{E}_{\pm j}^z = \pm D \frac{1-\Lambda^{-1}}{\ln \Lambda} \Lambda^{2-j-z} \quad (j = 2, 3, \ldots). \tag{46}$$

It is also straightforward to construct the functions φ_{jm}: substitution of Eq. (43) on the left-hand side of Eq. (36) yields

$$\mathcal{E}_j^z \int_{\ln(\epsilon_{j+1}^z/D)}^{\ln(\epsilon_j^z/D)} \varphi_{jm}^*(\epsilon) \varphi_{jm'}(\epsilon) d \ln(\epsilon/D) = \delta_{m,m'}, \tag{47}$$

which is satisfied by a Fourier series in the variable $\ln(\epsilon/D)$:

$$\varphi_{jm}(\epsilon) = \frac{\exp(2\pi i \omega_m)}{\sqrt{\mathcal{E}_j^z \ln \Lambda}} \quad (m \text{ integer}), \tag{48}$$

where

$$\omega_m = m \ln(\epsilon/D)/\ln \Lambda. \tag{49}$$

We can then compute the overlap between any two basis functions φ_{jm} ($m=0,1,\ldots$) and $\varphi_{jm'}$ ($m'=0,1,\ldots$). In particular, we find that

$$\left| \int_{I_j} \varphi_{jm}^*(\epsilon) \varphi_{j0}\, d\epsilon \right| = \frac{\ln \Lambda}{\sqrt{\ln^2 \Lambda + 4\pi^2 m^2}}, \tag{50}$$

which shows that, in the limit $\Lambda \to 1$, φ_{j0} becomes orthogonal to the other basis functions.

For each interval I_j, we therefore have that (i) since the conduction-band matrix elements $\mathcal{A}^j_{mm'}$ on the right-hand side of Eq. (41) vanish for $m' \neq m$, the operators a_{j0} are decoupled from the a_{jm} ($m \neq 0$); (ii) since, as Eq. (39) shows, the operator f_0 is a linear combination of the a_{j0}, the impurity is also decoupled from the a_{jm} ($m \neq 0$); (iii) although the basis is nonorthogonal, the overlap $\{a_{j0}^\dagger, a_{jm}\}$ ($m \neq 0$) vanishes in the continuum limit. These three findings suggest that, as an approximation, we neglect the operators $a_{jm}(m \neq 0)$ in Eq. (41) and write the model Hamiltonian as

$$H_A = \sum_j \mathcal{E}_j^z a_{j0}^\dagger a_{j0} + \sqrt{\frac{2D\Gamma}{\pi}}(f_0^\dagger c_{\text{imp}} + \text{H.c.}) + \epsilon_{\text{imp}} n^{\text{imp}} + U n_\uparrow^{\text{imp}} n_\downarrow^{\text{imp}}. \tag{51}$$

We are ready, now, to calculate the spectral density for the operator f_0 in the limit $\Gamma \to 0$. Notice taken of the similarity between Eqs. (16) and (51), we can reproduce the steps leading from the latter to Eq. (25), to find

$$\rho_0(\epsilon) = \frac{\epsilon_j - \epsilon_{j+1}}{2D|d\mathcal{E}_j^z/dz|_{\mathcal{E}_j=\epsilon}}. \tag{52}$$

From Eq. (46) we then evaluate the derivative on the right-hand side,

$$d\mathcal{E}_j^z/dz = D(\epsilon_j - \epsilon_{j+1}), \tag{53}$$

which reproduces Eq. (27):

$$\rho_0(\epsilon) = 1/2D. \tag{54}$$

This improvement over the result (33), derived in Sec. IV, is due to the weight function $g(\epsilon) \sim 1/\epsilon$. We can interpret the left-hand side of Eq. (36) as a scalar product calculated with the variable $x(\epsilon) \equiv \ln(\epsilon/D)$, instead of ϵ. Since $x(\epsilon_j) = (2-j-z)\ln \Lambda$, the function $g(\epsilon)$ effectively makes the energy limits linearly dependent on the twist parameter. This does not make Eq. (51) exact, but it treats the impurity-band coupling as accurately as a linear discretization would.

VI. TWO-IMPURITY MODEL

We now turn to the two-impurity Anderson model, whose Hamiltonian comprises energy-dependent impurity-band couplings. We will see that this dependency enhances the problem that Eq. (33) exposed. As illustrations, we will compare results for the impurity-added contribution to the specific heat and for the impurity spectral density calculated by the procedure in Sec. V with ones calculated by the procedure in Sec. IV.

The two-impurity Hamiltonian is

$$H_{A2} = \sum_{\vec{k}} \epsilon_k c_{\vec{k}}^\dagger c_{\vec{k}} + \epsilon_{\text{imp}} \sum_{j=1}^{2} n_j^{\text{imp}} + U \sum_{j=1}^{2} n_{j\uparrow}^{\text{imp}} n_{j\downarrow}^{\text{imp}} + V\left(\sum_{j,\vec{k}} e^{i\vec{k}\cdot\vec{R}_j} c_{\vec{k}}^\dagger c_j^{\text{imp}} + \text{H.c.} \right), \tag{55}$$

where the index j ($j=1,2$) denotes the two impurities, positioned at $\vec{R}_1 = -\vec{R}_2 = \vec{R}/2$, respectively.

Following by now standard procedure, we introduce parity-conserving conduction-band operators:[15]

$$c_{\epsilon+} = \left(\rho(\epsilon) \frac{1+S_\epsilon}{2} \right)^{-1/2} \sum_{\vec{k}} c_{\vec{k}} \cos \frac{\vec{k}\cdot\vec{R}}{2} \delta(\epsilon - \epsilon_k) \tag{56}$$

and

$$c_{\epsilon-} = i\left(\rho(\epsilon) \frac{1-S_\epsilon}{2} \right)^{-1/2} \sum_{\vec{k}} c_{\vec{k}} \sin \frac{\vec{k}\cdot\vec{R}}{2} \delta(\epsilon - \epsilon_k), \tag{57}$$

where

$$S_{\epsilon_k} \equiv \sin kR/kR, \tag{58}$$

and $\rho(\epsilon)$ is the per spin density of states, a constant in our model.

Expressed on the basis of the $c_{\epsilon\pm}$, the model Hamiltonian reads

$$H_{A2} = \sum_{p=\pm} \int_{-D}^{D} \epsilon c_{\epsilon p}^\dagger\, c_{\epsilon p} d\epsilon + \epsilon_{\text{imp}} \sum_{p=\pm} n_p^{\text{imp}} + U \sum_{j=1}^{2} n_{j\uparrow}^{\text{imp}} n_{j\downarrow}^{\text{imp}} + \sqrt{\frac{2D\Gamma}{\pi}} \sum_{p=\pm} (\sqrt{\bar{\gamma}_p} f_{0p}^\dagger c_p^{\text{imp}} + \text{H.c.}), \tag{59}$$

where $c_\pm^{\text{imp}} = (c_1^{\text{imp}} \pm c_2^{\text{imp}})/\sqrt{2}$, and

$$f_{0\pm} = \int_{-D}^{D} \sqrt{\gamma_\pm(\epsilon)} c_{\epsilon\pm}\, d\epsilon / \sqrt{\bar{\gamma}_\pm}, \tag{60}$$

with

$$\gamma_\pm(\epsilon) \equiv \frac{1 \pm S_\epsilon}{2}, \tag{61}$$

$$\bar{\gamma}_\pm \equiv \int_{-D}^{D} \gamma_\pm(\epsilon) d\epsilon. \tag{62}$$

and

$$\Gamma \equiv \pi \rho V^2. \tag{63}$$

We now follow the discretization procedure in Sec. V, but instead of Eq. (35), we introduce functions φ_{j0} ($j = \pm 1, \pm 2, \ldots$) adapted to Eq. (60):

$$\varphi_{j0\pm} = \left(\frac{\gamma_\pm(\epsilon)}{\int_{I_j} \gamma_\pm(\epsilon) d\epsilon} \right)^{1/2}, \tag{64}$$

so that when operators $a_{j0\pm} \equiv \int_{I_j} \varphi_{j0\pm}(\epsilon) c_{\epsilon\pm}\, d\epsilon$ are defined, a form analogous to Eq. (39) results:

$$f_{0\pm} = \sum_j \left(\frac{\int_{I_j} \gamma_\pm(\epsilon) d\epsilon}{\bar{\gamma}_\pm} \right)^{1/2} a_{j0\pm}. \tag{65}$$

As in Sec. V, for each interval $I_{j\pm}(j = \pm 1, \pm 2, \ldots)$, the modified orthogonality condition (36) allows the definition of other functions $\{\varphi_{jm\pm}(\epsilon)\}(m \neq 0)$, from which we can construct a nonorthogonal basis

$$a_{jm\pm} = \int_{I_{j\pm}} \varphi_{jm\pm}(\epsilon) c_\epsilon\, d\epsilon. \tag{66}$$

This relation inverted, we find expressions analogous to Eq. (40):

$$c_{\epsilon\pm} = \sum_{m=-\infty}^{\infty} g(\epsilon) \varphi_{jm\pm}(\epsilon) a_{jm\pm} \quad (\epsilon \in I_j). \tag{67}$$

The projection of the model Hamiltonian on this basis yields

$$H_{A2} = \sum_{jmm'p=\pm} \mathcal{A}^{jp}_{mm'} a^\dagger_{jmp} a_{jm'p} + \epsilon_{\text{imp}} \sum_{p=\pm} n^{\text{imp}}_p + U \sum_{j=1}^{2} n^{\text{imp}}_{p\uparrow} n^{\text{imp}}_{p\downarrow} + \sqrt{\frac{2D\Gamma}{\pi}} \sum_{p=\pm} (\sqrt{\bar{\gamma}_p} f^\dagger_{0p} c^{\text{imp}}_p + \text{H.c.}), \tag{68}$$

with conduction-band matrix elements

$$\mathcal{A}^{j\pm}_{mm'} = \int_{I_j} \varphi^*_{jm\pm}(\epsilon) \epsilon g^2(\epsilon) \varphi_{jm'\pm}(\epsilon) d\epsilon. \tag{69}$$

As in our treatment of Eq. (42), we choose $g(\epsilon) = \mathcal{E}^z_{j\pm}/\epsilon$, with $\mathcal{E}^z_{j\pm}$ such that

$$\int_{I_{j\pm}} |\varphi_{j0}|^2(\epsilon) g(\epsilon) d\epsilon = 1, \tag{70}$$

a condition that Eq. (64) turns into an explicit expression for the $\mathcal{E}^z_{j\pm}$ $(j = \pm 1, \pm 2, \ldots)$:

$$\mathcal{E}^z_{j\pm} = \frac{\int_{I_{j\pm}} \gamma_\pm(\epsilon) d\epsilon}{\int_{I_{j\pm}} \gamma_\pm(\epsilon) d\epsilon/\epsilon}. \tag{71}$$

Equation (69) then becomes

$$\mathcal{A}^{j\pm}_{mm'} = \delta_{mm'} \mathcal{E}^z_{j\pm}, \tag{72}$$

and hence, as in Eq. (51), we keep only the term with $m = m' = 0$ in the sum on the right-hand side of Eq. (68):

$$H_{A2} = \sum_{jp=\pm} \mathcal{E}^z_{jp} a^\dagger_{j0p} a_{j0p} + \epsilon_{\text{imp}} \sum_{p=\pm} n^{\text{imp}}_p + U \sum_{j=1}^{2} n^{\text{imp}}_{p\uparrow} n^{\text{imp}}_{p\downarrow} + \sqrt{\frac{2D\Gamma}{\pi}} \sum_{p=\pm} (\sqrt{\bar{\gamma}_p} f^\dagger_{0p} c^{\text{imp}}_p + \text{H.c.}). \tag{73}$$

Following the standard NRG treatment, we now construct two orthonormal infinite sequences of Fermi operators $f_{n\pm}$ $(n = 0, 1, \ldots)$, starting with the $f_{0\pm}$ in Eq. (65). A Lanczos transformation[16] applied to the first term on the right-hand side of Eq. (73) then determines the remaining operators and the diagonal (η_n) and codiagonal (t_n) matrix elements of the transformed Hamiltonian:[1,2,6,9]

$$H_{A2} = \sum_{np=\pm} [\eta_n f^\dagger_{np} f_{np} + t_n (f^\dagger_{np} f_{n+1p} + \text{H.c.})] + \epsilon_{\text{imp}} \sum_{p=\pm} n^{\text{imp}}_p + U \sum_{j=1}^{2} n^{\text{imp}}_{p\uparrow} n^{\text{imp}}_{p\downarrow} + \sqrt{\frac{2D\Gamma}{\pi}} \sum_{p=\pm} (\sqrt{\bar{\gamma}_p} f^\dagger_{0p} c^{\text{imp}}_p + \text{H.c.}). \tag{74}$$

The diagonal and codiagonal coefficients, which have to be calculated numerically,[6,9] diminish rapidly as n increases: $\eta_n \sim D\Lambda^{-n}$ and $t_n \sim D\Lambda^{-n/2}$.

To calculate a physical property at a temperature T or an energy ϵ, then, we choose a dimensionless parameter $\alpha \ll 1$ and neglect all η_n and t_n for $n > N$, where N is the smallest integer such that

$$D\Lambda^{-N/2} < \alpha k_B T, \tag{75}$$

where k_B is Boltzmann's constant, or

$$D\Lambda^{-N/2} < \alpha\epsilon, \tag{76}$$

respectively.

We then define a truncated, scaled Hamiltonian[18]

$$H^N_{A2} = \left(\sum_{n=0}^{N} \sum_{p=\pm} \eta_n f^\dagger_{np} f_{np} + \sum_{n=0}^{N-1} t_n (f^\dagger_{np} f_{n+1p} + \text{H.c.}) + \epsilon_{\text{imp}} \sum_{p=\pm} n^{\text{imp}}_p + U \sum_{j=1}^{2} n^{\text{imp}}_{j\uparrow} n^{\text{imp}}_{j\downarrow} + \sqrt{\frac{2D\Gamma}{\pi}} \sum_{p=\pm} (\sqrt{\bar{\gamma}_p} f^\dagger_{0p} c^{\text{imp}}_p + \text{H.c.}) \right) \frac{\Lambda^{(N-1)/2}}{D}, \tag{77}$$

so that the smallest scaled codiagonal coefficient on the right-hand side is of the order of unity: $t_{N-1}\Lambda^{(N-1)/2}/D \approx 1$. In the limit $N \to \infty$, we recover the discretized Hamiltonian $H_{A2} = \Lambda^{-(N-1)/2} H^N_{A2}$.

The numerical, iterative diagonalization of the truncated, scaled Hamiltonian gives access to the L lowest eigenvalues and eigenvectors of $H^N_{A2}(N = 0, 1, \ldots, N_{\max})$, and to matrix elements between those eigenstates.[2] The computational cost grows as the cubic power of the parameter L and linearly with the parameter $N_{\max}$. The former fixes the accuracy of the resulting physical properties and the latter, the minimum energy or temperature at which properties can be calculated.

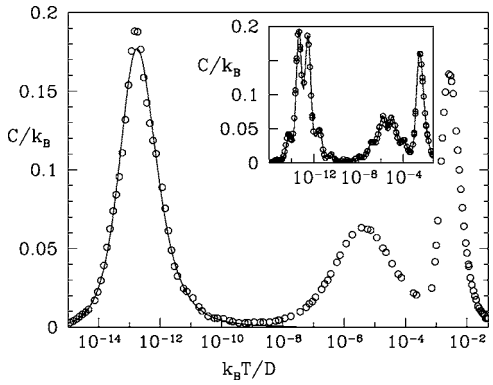

FIG. 1. Specific heat for the symmetric two-impurity Anderson model with the parameters $\Gamma=5\pi/4D$, $\epsilon_{\rm imp}=-50D$, $U=100D$, and $k_FR=\pi/2$, chosen so that the model maps onto a two-impurity Kondo model with (antiferromagnetic) coupling $J=0.1D$. The open circles in the main plot (in the inset) show the specific heats that Eq. (78) yields with the alternative procedure in Sec. V (with the traditional procedure). In the inset, the solid lines guide the eye. In the main plot, the solid line is the universal curve for the specific heat of the single-impurity Kondo model (Ref. 19). In each case, the Hamiltonian was diagonalized with $\Lambda=10$ and four z's, $z=0.25$, 0.5, 0.75, and 1.0, and the calculated specific heats were averaged over z.

VII. SPECIFIC HEAT

As a first example, we describe the computation of the impurity-added contribution to the specific heat. At a given temperature T, Eq. (75) yields the iteration number N at which the specific heat is to be calculated:[2,4,17]

$$C_{\rm imp}(T)=k_B\beta^2(\langle E^2\rangle-\langle E\rangle^2-\langle E^2\rangle_0-\langle E\rangle_0^2), \tag{78}$$

where $\beta=1/k_BT$ and the angular brackets denote thermal averages, e.g.,

$$\langle E\rangle=\frac{\mathrm{tr}[\exp(-\beta H_{A2}^N)H_{A2}^N]}{\mathrm{tr}[\exp(-\beta H_{A2}^N)]} \tag{79}$$

and

$$\langle E\rangle_0=\frac{\mathrm{tr}[\exp(-\beta H_0^N)H_0^N]}{\mathrm{tr}[\exp(-\beta H_0^N)]}, \tag{80}$$

where H_0^N is the conduction-band Hamiltonian, i.e., the sum of the first two terms on the right-hand side of Eq. (77).

Figure 1 compares the specific heats for the two-impurity Anderson model, in the Kondo limit, calculated with the discretization procedures in Secs. IV (insert) and V (main plot). In each case, the impurity-added contribution to the specific heat, calculated with Eq. (78) for $\Lambda=10$ and given z (not shown), exhibits artificial oscillations with amplitudes of the order of unity and period $\ln\Lambda$. In order to eliminate those oscillations, we have averaged the results over four z's, $z=0.25$, 0.5, 0.75, and 1.0. As the inset shows, even after averaging, the traditional procedure yields specific heat curves with remanescent oscillations, ultimately due to its inaccurate handling of the operators $f_{0\pm}$. By contrast, the alternative procedure in Sec. V yields the well-defined peaks shown in the main plot, whose physical interpretation has been presented in Ref. 13. Although, at temperatures below $10^{-10}D$, deviations from the universal Kondo peak[19] are still visible, the discrepancies are substantially smaller than those in the inset and can be eliminated by averaging the results with curves obtained with different Λ's. In particular, the specific heat temperature dependencies reported in Ref. 13 resulted from averaging curves calculated with $\Lambda=10$ and 9.

VIII. IMPURITY SPECTRAL DENSITIES

As a second illustration, we turn to the even and odd impurity spectral densities $\rho_\pm^{\rm imp}$ for the uncorrelated ($U=0$) model, a choice dictated by two practical considerations: (i) the continuum limit of $\rho_\pm^{\rm imp}$ can be computed analytically; (ii) in numerical computations of $\rho_\pm^{\rm imp}$ for $\Lambda\geqslant 2$, only the discretization introduces significant deviations. It follows that the difference between the numerical results and the continuum limit measures the accuracy of the discretization procedure.

When $U=0$, the continuum Hamiltonian, Eq. (59), is decoupled into an even and an odd terms, each of which can be diagonalized analytically. The (per spin) impurity spectral densities, which in the notation of Eq. (22) are defined as

$$\rho_\pm^{\rm imp}(\epsilon)=\begin{cases}\displaystyle\sum_\alpha |\langle\alpha|c_\pm^{\rm imp}|\Omega\rangle|^2\delta(E_\alpha-E_\Omega+\epsilon) & (\epsilon<0),\\ \displaystyle\sum_\alpha |\langle\Omega|c_\pm^{\rm imp}|\alpha\rangle|^2\delta(E_\alpha-E_\Omega-\epsilon) & (\epsilon>0),\end{cases} \tag{81}$$

can accordingly be expressed in closed form:

$$\rho_\pm^{\rm imp}(\epsilon)=\frac{1}{\pi}\frac{\Gamma_\pm(\epsilon)}{\Gamma_\pm^2(\epsilon)+[\epsilon-\epsilon_\pm^*(\epsilon)]^2}, \tag{82}$$

where

$$\Gamma_\pm(\epsilon)\equiv 2\Gamma\gamma_\pm(\epsilon) \tag{83}$$

is the effective, channel-dependent impurity width, and

$$\epsilon_\pm^*(\epsilon)=\epsilon_{\rm imp}-\mathcal{P}\int\frac{1}{\pi}\frac{\Gamma_\pm(\epsilon')}{\epsilon'-\epsilon}d\epsilon' \tag{84}$$

is the self-interaction-corrected impurity energy.

When $U=0$, moreover, the numerical procedure is also simplified. The Hamiltonian (77) decouples into an even component H_{A+}^N and an odd one H_{A-}^N, each a quadratic form:

$$H_{A\pm}^N=\mathcal{F}^\dagger\mathcal{H}_\pm^N\mathcal{F}, \tag{85}$$

where $\mathcal{F}$ is a vector comprising $N+2$ Fermi operators:

$$\mathcal{F}\equiv(c^{\rm imp}f_0f_1\cdots f_N), \tag{86}$$

and $\mathcal{H}_\pm^N$, is an $(N+2)\times(N+2)$ matrix

$$\mathcal{H}_{\pm}^{N}=\begin{bmatrix} \epsilon_{\mathrm{imp}} & \sqrt{\frac{2D\Gamma\bar{\gamma}_{\pm}}{\pi}} & 0 & \cdots & 0 \\ \sqrt{\frac{2D\Gamma\bar{\gamma}_{\pm}}{\pi}} & \eta_{0\pm} & t_{0\pm} & \cdots & 0 \\ 0 & t_{0\pm} & \eta_{1\pm} & \cdots & 0 \\ 0 & 0 & t_{1\pm} & \cdots & 0 \\ \vdots & \vdots & \vdots & \vdots & \vdots \\ 0 & 0 & 0 & \cdots & \eta_{N\pm} \end{bmatrix} \frac{\Lambda^{(N-1)/2}}{D}. \tag{87}$$

For the N's of interest, typically well below 50, the numerical diagonalization of the $\mathcal{H}_{\pm}^{N}$ is trivial. From the resulting eigenvectors, one can easily calculate the matrix elements needed to compute the impurity spectral densities (81). Unlike the iterative diagonalization, which keeps a limited number of states L at each step and hence introduces truncation errors, the diagonalization of the quadratic form (85) considers all the states on the basis of the operators c^{imp}, f_n $(n=0,1,\ldots,N)$, and is affected only by the discretization.

For given z, thus, we diagonalize the matrix on the right-hand side of Eq. (87) numerically. The resulting eigenvectors $v_{m\pm}\equiv[\alpha_{\mathrm{imp}}^{m\pm}(z),\alpha_{0}^{m\pm}(z),\ldots,\alpha_{N}^{m\pm}(z)]$ $(m=1,,\ldots,N+2)$ yield the Fermi operators

$$g_{m\pm}^{z}=\alpha_{\mathrm{imp}}^{m\pm}(z)c^{\mathrm{imp}}+\sum_{n=0}^{N}\alpha_{n}^{m\pm}(z)f_{n}, \tag{88}$$

which diagonalize $H_{A\pm}^{N}$.

Inversion of Eq. (88) yields

$$c_{\pm}^{\mathrm{imp}}=\sum_{m=1}^{N+2}\alpha_{\mathrm{imp}}^{m\pm}g_{m\pm}, \tag{89}$$

and substitution in Eq. (81) leads to the z-dependent spectral density

$$\rho^{\mathrm{imp}}(\epsilon,z)=\sum_{m=1}^{N+2}|\alpha_{\mathrm{imp}}^{m\pm}(z)|^{2}\delta[E_{m\pm}(z)-|\epsilon|]. \tag{90}$$

As in Sec. IV, we now have to integrate over the twist parameter to eliminate the spikes on the right-hand side:

$$\rho^{\mathrm{imp}}(\epsilon)\equiv\int_{0}^{1}\rho_{\pm}^{\mathrm{imp}}(\epsilon,z)dz, \tag{91}$$

which yields

$$\rho^{\mathrm{imp}}(\epsilon)=\sum_{m=1}^{N+2}\frac{|\alpha_{\mathrm{imp}}^{m\pm}(z)|^{2}}{(dE_{m\pm}/dz)_{E_{m\pm}(z)=\epsilon}}. \tag{92}$$

Figures 2 and 3 depict the impurity spectral densities $\rho_{\pm}^{\mathrm{imp}}(\epsilon)$ for the two-impurity Anderson model with the following parameters: width $\Gamma=9\pi\times10^{-4}D$, impurity energy $\epsilon_{\mathrm{imp}}=-0.01D$, impurity separation $R=\pi/2k_F$, and $U=0$. The former shows the odd spectral density in the energy range $-10^{-4}D>\epsilon>-10^{-1}D$, which surrounds the resonance in Eq. (82). Since at such low energies the parameter S_{ϵ} in Eq. (58) is approximately 0.6, the effective width Γ_{-} is substantially smaller than Γ, and the odd spectral density shows an enhanced, narrow peak. As indicated by the crosses, the NRG diagonalization of the model Hamiltonian discretized by the procedure in Sec. IV, with a renormalized impurity-level width $\Gamma_{\mathrm{numerical}}=A_{\Lambda}\Gamma$, yields spectral densities in good agreement with Eq. (82). The inset shows deviations separating the crosses from the solid line that are smaller than 1% of the peak, hence well within the standard tolerance—3% of the maximum—for NRG computations.

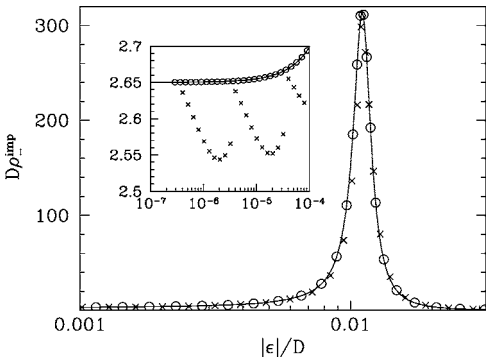

FIG. 2. Odd impurity spectral density for the uncorrelated Anderson Hamiltonian Eq. (59) for $U=0$, with the parameters $\Gamma=9\pi\times10^{-4}D$, $\epsilon_{\mathrm{imp}}=-0.01D$, and $k_FR=\pi/2$. The solid line represents the exact density Eq. (82). The crosses and the circles are the results of NRG diagonalizations of the model Hamiltonian discretized with the procedures in Secs. IV and V, respectively. In the former diagonalization, the parameter Γ was multiplied by the factor A_{Λ}, defined by Eq. (34). With enhanced vertical resolution, the inset shows the low-energy tail of the curves to make visible the deviations separating the numerical results from the exact curve.

Although the traditional procedure yields relatively small deviations, the alternative procedure is remarkably more accurate. The circles in Fig. 2, which represent the energy dependence of the odd spectral density resulting from the NRG diagonalization of the model Hamiltonian, with unrenormalized parameters, discretized by the method in Sec. V, are indistinguishable, on the scale of the inset, from the exact curve.

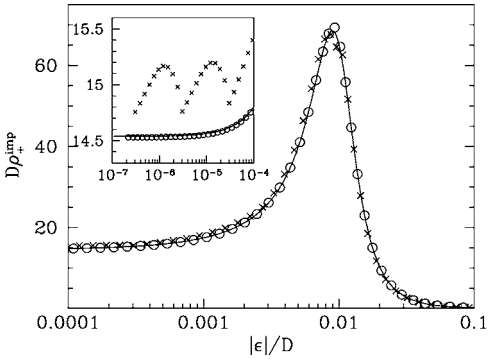

FIG. 3. Even impurity spectral density for the Anderson Hamiltonian, with the parameters and symbols defined in Fig. 2. The broader, less pronounced peak reflects the larger effective impurity width $\Gamma_{+}\approx\Gamma$. With enhanced resolution, the inset displays the low-energy tail of the curves.

Figure 3 follows the same symbol convention to display the even spectral density in the same energy interval. The even effective width Γ_+ is close to Γ, so that the peak near $\epsilon=\epsilon_{\rm imp}$ is broader and lower than the one in Fig. 2. The two NRG curves again agree well with Eq. (82). As demonstrated by the blown-up view of the low-energy region in the inset, the deviations separating the crosses from the solid curve are now 1% of the peak density and hence fit less comfortably within the standard NRG tolerance; for larger impurity widths, the deviations would exceed that tolerance. By contrast, the circles display excellent agreement with the exact curve.

The discrepancies between the crosses and the solid line in the insets of Figs. 2 and 3 reflect a shortcoming of the traditional procedure, which yields impurity self-energies that converge slowly to the continuum limit. To see this, consider the even and the odd self-energies at the Fermi level, derived from Eq. (59):

$$\Sigma_{{\rm imp}\pm}(\epsilon=0)=-\mathcal{P}\int_{-D}^{D}\frac{2\Gamma\bar{\gamma}_\pm}{\pi}\frac{\{c_{\epsilon'}^\dagger,f_{0\pm}\}^2}{\epsilon'}d\epsilon'. \tag{93}$$

When the anticommutator in the integral on the right-hand side is computed from Eq. (60), we find the continuum-limit self-energies:

$$\Sigma_{{\rm imp}\pm}(\epsilon=0)=-\frac{2\Gamma}{\pi}\mathcal{P}\int_{-D}^{D}\frac{\gamma_\pm(\epsilon')}{\epsilon'}d\epsilon'. \tag{94}$$

Consider, next, the computation of the self-energies for the discretized Hamiltonian (73), again with $U=0$. Instead of Eq. (94), we now have that

$$\Sigma_{{\rm imp}\pm}^{\rm NRG}(\epsilon=0)=-{\sum_{j=-\infty}^{\infty}}'\frac{2\Gamma\bar{\gamma}_\pm}{\pi}\frac{\{a_{j\pm}^\dagger,f_{0\pm}\}^2}{\mathcal{E}_{j\pm}}, \tag{95}$$

where the prime reminds us that the $j=0$ term is excluded from the sum on the right-hand side. The anticommutator on the right-hand side computed from Eq. (65), and the right side of Eq. (71) substituted for the energies $\mathcal{E}_{j\pm}$, we find that

$$\Sigma_{{\rm imp}\pm}^{\rm NRG}(\epsilon=0)=-\frac{2\Gamma}{\pi}{\sum_{j=-\infty}^{\infty}}'\int_{I_j}\frac{\gamma_\pm(\epsilon')}{\epsilon'}d\epsilon'. \tag{96}$$

Since the juxtaposition of the intervals I_j reproduces the conduction band, Eqs. (94) and (96) are equivalent; for any Λ and z, the procedure in Secs. V and VI yields exact self-energies.

In the traditional approach, while $f_{0\pm}$ is still related to the the discrete conduction operators $a_{j\pm}$ ($j=\pm1,\pm2,\ldots$) by Eq. (65), the discrete conduction energies are no longer given by Eq. (71). Instead, in analogy with Eq. (17), we have that

$$E_{j\pm}=\frac{\displaystyle\int_{I_{j\pm}}\epsilon\gamma_\pm(\epsilon)d\epsilon}{\displaystyle\int_{I_{j\pm}}\gamma_\pm(\epsilon)d\epsilon}\quad(j=1,2,\ldots). \tag{97}$$

Substitution of these energies for the $\mathcal{E}_{j\pm}$ on the right-hand side of Eq. (95) then leads to the self-energies calculated by the traditional procedure:[20]

$$\Sigma_{{\rm imp}\pm}^{\rm trad}(\epsilon=0)=-\frac{2\Gamma}{\pi}{\sum_{j=-\infty}^{\infty}}'\frac{\left[\displaystyle\int_{I_j}\gamma_\pm(\epsilon')d\epsilon'\right]^2}{\displaystyle\int_{I_j}\gamma_\pm(\epsilon')d\epsilon'/\epsilon'}. \tag{98}$$

Only in the continuum limit does this relation reproduce Eq. (94). For $\Lambda>1$, the right-hand side depends on both Λ and z. Spectral densities computed with the traditional procedure deviate from the continuum limit; moreover, since spectral densities at different energies ϵ are computed with different z's [cf. Eq. (92)], the deviations depend on ϵ, as the crosses in the insets of Figs. 2 and 3 show.

Although our discussion of the impurity spectral densities has been restricted to the $U=0$ model, it is in principle straightforward to apply Eqs. (81) and (91) to the correlated model.[4] In practice, however, in addition to coupling H_{A+} to H_{A-}, the correlation makes quadratic factorizations such as that on the right-hand side of Eq. (85) impossible. As a result, the model Hamiltonian must be diagonalized iteratively. Since the number of eigenstates $|\alpha\rangle$ that Eq. (81) requires at each iteration is substantially larger than that required by Eqs. (78)–(80), even the coarse logarithmic mesh ($\Lambda=10$) in Sec. VII is insufficient to bring the necessary numerical effort within the limitations of our current computational resources. We therefore defer to future work the computation of the spectral densities for the correlated two-impurity Anderson model.

IX. CONCLUSIONS

An essential ingredient of NRG computations is the projection of conduction-band Hamiltonians on an incomplete discrete basis, an approximation controlled by the discretization parameter Λ and justified by the remarkably rapid convergence of calculated physical properties to the continuum limit. Fast convergence, it has long been realized, requires *ad hoc* renormalization of the impurity-band coupling by the factor A_Λ, defined in Eq. (34).[2] As shown by Eq. (33), this correction is needed to compensate for a shortcoming of the logarithmic discretization, which underestimates the spectral density ρ_0 associated with the coupling. Energy-dependent couplings, such as those found in the two-impurity Anderson Hamiltonian, make the renormalization energy dependent, and hence push the problem beyond the scope of *ad hoc* corrections.

Section V introduced an alternative discretization that evaluates ρ_0 correctly and hence allows computations of the physical properties for models with energy-independent couplings based on the bare values of the coupling constants. For energy-dependent couplings, it guarantees fast convergence to the continuum limit. The alternative expression for the discretized energies, of which Eq. (44) is an illustration, is therefore superior to the standard formula, illustrated by

Eq. (17). Since the integrals involved in the former expression are no more demanding than those in the latter, this procedure is as practical as and more accurate than the traditional one.

ACKNOWLEDGMENTS

This work was supported by the Brazilian agencies FAPESP, CNPq, and CAPES.

[1] K. G. Wilson, Rev. Mod. Phys. **47**, 773 (1975).
[2] H. R. Krishna-murthy, J. W. Wilkins, and K. G. Wilson, Phys. Rev. B **21**, 1003 (1980).
[3] H. R. Krishna-murthy, J. W. Wilkins, and K. G. Wilson, Phys. Rev. B **21**, 1044 (1980).
[4] H. O. Frota and L. N. Oliveira, Phys. Rev. B **33**, R7871 (1986).
[5] B. A. Jones and C. M. Varma, Phys. Rev. Lett. **58**, 843 (1987).
[6] M. Yoshida, M. A. Whitaker, and L. N. Oliveira, Phys. Rev. B **41**, 9403 (1990).
[7] T. Costi, A. Hewson, and V. Zlatic, J. Phys.: Condens. Matter **6**, 2519 (1994).
[8] A. C. Hewson, *The Kondo Problem to Heavy Fermions* (Cambridge University Press, Cambridge, U.K., 1993).
[9] K. Chen and C. Jayaprakash, Phys. Rev. B **52**, 14436 (1995).
[10] J. B. Silva, W. L. C. Lima, W. C. Oliveira, J. L. N. Mello, L. N. Oliveira, and J. W. Wilkins, Phys. Rev. Lett. **76**, 275 (1996).
[11] R. Bulla, T. Pruschke, and A. C. Hewson, J. Phys.: Condens. Matter **9**, 10463 (1997).
[12] W. Hofstetter, Phys. Rev. Lett. **85**, 1508 (2000).
[13] V. L. Campo, Jr., and L. N. Oliveira, Phys. Rev. B **70**, 153401 (2004).
[14] As pointed out in Ref. 2, A_Λ converges rapidly to unity as $\Lambda \to 1$. Nonetheless, even for Λ as small as 2, the renormalization of the coupling constant $\sqrt{\Gamma}$ can change the Kondo temperature, which decays exponentially with U/Γ, by orders of magnitude.
[15] C. Jayaprakash, H. R. Krishna-Murthy, and J. W. Wilkins, Phys. Rev. Lett. **47**, 737 (1981).
[16] L. Komzsik, *The Lanczos Method: Evolution and Application* (SIAM, Philadelphia, 2003).
[17] W. C. Oliveira and L. N. Oliveira, Phys. Rev. B **49**, 11986 (1994).
[18] The procedure in Sec. V modifies the diagonal and the codiagonal elements in Eq. (77) with respect to those in the traditional approach. For uniform impurity-band couplings, the modification amounts to multiplication by a constant, $t_n \to t_n/A_\Lambda$, and is therefore equivalent to a change in the model parameters. For energy-dependent couplings, however, as Figs. 1–3 show, the change in the t_n's and η_n's alters the temperature (energy) dependence of thermodynamic (dynamic) properties.
[19] A. M. Tsvelick and P. B. Wiegmann, Adv. Phys. **32**, 453 (1983).
[20] For energy-independent couplings, i.e., for constant $\gamma_\pm(\epsilon)$, Eq. (98) becomes equivalent to Eq. (96) with $\Gamma \to \Gamma/A_\Lambda$, yet another example of the renormalization of the coupling constant.